Autonomous Spectral Discovery and Mapping Onboard the EO-1 Spacecraft

David R. Thompson[1,2], Benjamin J. Bornstein[2], Steve A. Chien[2], Steve Schaffer[2], Daniel Tran[2], Brian D. Bue[3], Rebecca Castaño[2], Damhnait Gleeson[4], Aaron Noell[2]

Abstract—Imaging spectrometers are valuable instruments for space exploration, but their large data volumes limit the number of scenes that can be downlinked. Missions could improve science yield by acquiring surplus images and analyzing them onboard the spacecraft. This onboard analysis could generate surficial maps, summarizing scenes in a bandwidth-efficient manner to indicate data cubes that warrant a complete downlink. Additionally, onboard analysis could detect targets of opportunity and trigger immediate automated followup measurements by the spacecraft. Here we report a first step toward these goals with demonstrations of fully automatic hyperspectral scene analysis, feature discovery and mapping onboard the EO-1 spacecraft. We describe a series of overflights in which the spacecraft analyzes a scene and produces summary maps along with lists of salient features for prioritized downlink. The onboard system uses a superpixel endmember detection approach to identify compositionally distinctive features in each image. This procedure suits the limited computing resources of the EO-1 flight processor. It requires very little advance information about the anticipated spectral features, but the resulting surface composition maps agree well with canonical human interpretations. Identical spacecraft commands detect outlier spectral features in multiple scenarios having different constituents and imaging conditions.

Index Terms—Endmember detection, Hyperspectral Imagery, Pattern Recognition, Spacecraft Autonomy, Remote Planetary Geology, Mineralogy

I. INTRODUCTION

Imaging spectrometers provide information about surface composition over wide areas along with morphological context. This rich information makes them highly valuable for planetary exploration. Noteworthy examples include the Moon Mineralogy Mapper (M^3) [1], and the Compact Reconnaissance Imaging Spectrometer at Mars (CRISM) [2], [3]. Future missions could use imaging spectrometers for an even wider range of targets including volatiles or mineralogically-distinctive units on asteroids [4], anomalous exposures during rover site surveys of Mars [5], atmospheric phenomena measured by outer planet orbiters [6], and organic materials on icy bodies [7]. Imaging spectrometers could also play a role in cubesat-scale exploration [8]. Unfortunately these sensors require a high data volume, and communications bandwidth cannot typically support the maximum imaging rate.

For example, the CRISM investigation will return multiple Terabytes of data but cover only a very small fraction of the planet's surface at full resolution. Overall, extreme bandwidth requirements limit imaging spectrometers to a small fraction of their potential duty cycles.

Onboard data analysis could help address this challenge. Spacecraft could acquire spectra at the maximum imaging rate, analyze the result onboard, and detect important features for priority downlink. The onboard analysis could ensure that ground operators do not miss anomalies of scientific interest. Spacecraft could draft mineralogical maps describing scene constituents using a small fraction of the normal data volume [9]. Such summary products could inform operator decisions about which of the full-resolution data cubes to retrieve from the spacecraft. Finally, onboard feature recognition could trigger immediate spacecraft responses such as followup observations at higher resolution [10]. In this fashion a spacecraft could respond directly to targets of opportunity, overcoming the delay of round-trip communications and spacecraft command sequencing [11]. Overall, onboard analysis could make imaging spectrometers applicable to a wider range of missions and multiply their yield in current exploration applications.

Real time hyperspectral feature discovery in planetary scenarios is a challenging problem, with unique difficulties that exclude many techniques developed for ground-based or airborne analyses. First, unexpected spectral shapes are often observed so the retrieval algorithms should not be too specific or limited only to known targets. Most terrestrial mapping methods rely on examples drawn from previous images, laboratory or in situ spectra. This is not always appropriate for planetary exploration, where spectra could vary significantly due to substrate, ambient temperature, atmospherics and mineralogy. We also desire the ability to discover and map features that have not yet been seen before.

Second, planetary hyperspectral images are generally noisier than terrestrial and airborne data. Orbitally-acquired spectra have intrinsically low Signal to Noise Ratios (SNRs), and often contain non-Gaussian artifacts from their harsh thermal and radiation environments. This has led planetary image analysts to a variety of special methods such as averaging over large spatial regions to reduce noise, and ratioing to improve the contrast of spectral features [3], [12], [13]. Applying these methods effectively requires considerable human artistry and direction. Authoritative interpretations may require days of attention by a trained analyst. Autonomous explorer spacecraft must provide the essential information required to permit these interpretations, but without the benefit of operator oversight.

The system must have a minimum of free parameters, and it should function effectively for all scenes on the first try.

Finally, spacecraft power and computational resources are highly constrained. Volatile memory is limited, and flight processors are often orders of magnitude slower than the terrestrial state of the art. This precludes most typical analysis pipelines. Recent efforts have turned to dedicated hardware, with numerous ground-side simulations using Field Programmable Gate Array (FPGA) coprocessors to perform endmember discovery [14]–[17], spectral unmixing [18], matched filter target detection [19], and compression [20], [21]. However, software implementations could still be important for cubesat-scale missions with constraints on system complexity, mass and power consumption [22]. Software implementations can also play an important role for spacecraft retrofits and "extended mission" demonstrations on existing spacecraft hardware. Consequently computational efficiency remains a key challenge for an initial proof of concept.

This work demonstrates automatic feature discovery and scene summary onboard the Earth Observing One (EO-1) spacecraft. We apply a superpixel endmember detection approach to detect spectrally-distinctive features [23], [24]. The spacecraft acquires an image, automatically segments and analyzes the image to detect spectral endmembers, and then forms a simple compositional map. The system can process an entire image using EO-1's 12MHz fixed-point flight processor and only 16MB of volatile memory. The resulting summary product describes the entire scene contents using the endmember features and the map. This 20KB summary reduces the raw data to less than 1% of its original volume. Nevertheless it preserves relevant spectral and spatial information about the key constituents and as well as anomalous outliers. The analysis is based on intrinsic properties of the scene, and thus does not require prior knowledge of the features that will be observed. Under these difficult constraints the result still resembles canonical maps produced using accurate airborne data and field expertise.

The following section describes the flight algorithm and approach. The subsequent section describes experiments that took place over repeated trials during the period of September 2011 to February 2012. We examine overflight acquisitions of several scenes of mineralogical and scientific interest, and compare the downlinked results from the onboard system to typical expert analyses. Finally, we close with a discussion of potential improvements and applications.

II. APPROACH

The Earth Observing One (EO-1) spacecraft has been in continuous operations since November 2000. It hosts the hyperspectral imager Hyperion, the first imaging spectrometer to operate from space. It has produced over 30,000 images of the Earth's land surface and oceans. The scenes have a spatial footprint of 7.5km across track and nearly 100km down track, with a resolution of approximately 30 meters per pixel at nadir, a spectral resolution of 0.38 to 2.5μm wavelengths, and channel widths of approximately 10nm Full Width at Half Maximum (FWHM) [25]. Its primary applications include

geology, mineralogy, land use mapping, and ocean color analyses.

Since 2004, EO-1's extended mission has also pioneered a range of autonomy software. The Autonomous Sciencecraft Experiment [26] enables onboard processing of Hyperion instrument data to detect science events and features. These include thermal hotspots corresponding to volcanism [27], cryosphere [28], flooding [29], and sulfur [30]. The data analysis involves classifying individual pixels into discrete types such as snow, water, ice, land, and clouds. Operators construct classifiers in advance using libraries of collected images. At runtime, the onboard detection enables autonomous response in the form of an alert message, prioritized downlink of science products or subimages, and possibly followup acquisitions on a later overflight.

There are many diverse methods for hyperspectral signal detection and mapping, but not all methods in current use are suitable for fully-automatic spacecraft operations. The CRISM mineral indices [31] typify classification rules constructed from band ratios and geometric depths of absorption features; they yield numerical scores which suggest the abundance of known target minerals and absorption features. Tetracorder [32] is a comprehensive classification and mapping system based on an expert system combined with a library of spectra. Other analysis strategies include Support Vector Machines (SVMs) or other machine learning approaches. These are generally tuned to specific classes and require extensive training sets, though some recent advances have been made with library spectra [33]. Finally, matched filtering and partial unmixing methods such as Mixture Tuned Matched Filtering [34] detect specific target signatures using an estimate of the scene background.

The goal of this work was to demonstrate a more general analysis technique that would map and summarize components of a scene without requiring advance training or a target signature library. We favor automatic *endmember detection and mapping* [35] to summarize constituents and outlier features based on intrinsic scene constituents alone. We treat the Hyperion observed spectrum as a vector of reflectance measurements at different wavelengths $s \in R^n$. Under a simple aereal linear mixing model [36] the observed reflectance spectrum is the product of a matrix $\mathbf{E}$ whose rows are spectral endmembers, with a vector of nonnegative mixing coefficients $\mathbf{u}$, subject to a noise term N. For simplicity N is typically assumed to be zero-mean Gaussian distribution.

$$s = \mathbf{E}\mathbf{u} + \mathcal{N} \qquad (1)$$

Assuming the actual undiluted endmembers are all present in the image, their locations and spectra can summarize the scene. They indicate main constituents as well as outliers representing compositionally distinctive features of scientific interest. Furthermore, endmember spectra can easily be subjected to post-analyses by a classifier, library, or matched filter to ascribe semantic interpretation and automatically schedule appropriate followup activities [37].

For these reasons, and because it makes few assumptions about the target spectra, automatic endmember detection [35], [36] is a compelling option for scene summary. Thorough
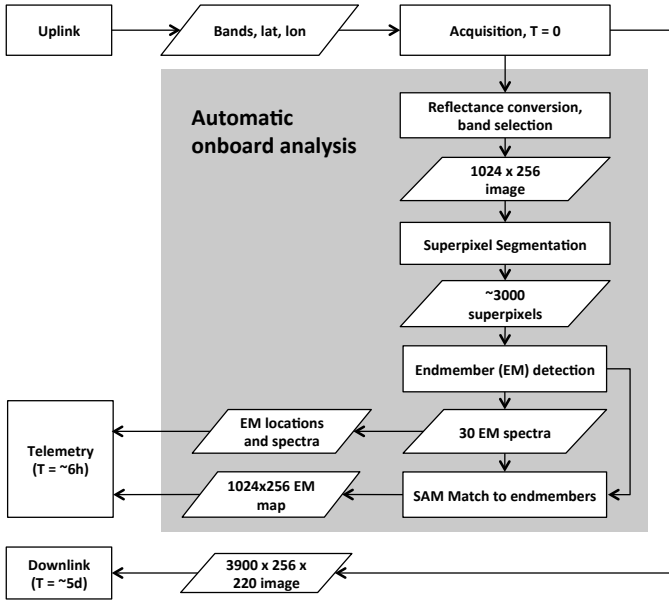
Fig. 1. Architecture for automatic spectral discovery and mapping on EO-1. The traditional operations approach involves a *slow path* for caching and downlink of large data volume full images (outside loop). The new onboard system permits faster downlinks of lightweight summary products in regular telemetry; this could potentially improve the effective coverage and turnaround time.

reviews of these algorithms can be found in [38] and [39]. Popular algorithms include the Pixel Purity Index (PPI) approach, which looks for extreme pixels in random linear projections [40]; N-FINDR [41], which looks for the subset of pixels defining the largest volume; and Vertex Component Analysis (VCA) [42], which grows an endmember set by computing the subspace spanned by the current set and projecting the data onto a new orthogonal direction. These methods are all somewhat sensitive to noise since numerical outliers often appear as endmembers. Hyperion pixels, like spacecraft hyperspectral imagers in general, suffer from some level of noise – both single-pixel errors, channel errors, as well as column striping effects. Here we detail an automatic scene summary that has favorable computational efficiency and reliably detects physical endmembers in the presence of noisy pixels. We exploit the spatial dimension similar to previous work by [43]–[45]. Specifically, we use a superpixel endmember detection approach described previously in work by Thompson et al [23].

Figure 1 shows the system architecture. Retrieving a full spectral image from EO-1 flight recorder typically requires several days for queuing and transmission. This is also typical for exploration missions. In contrast, the onboard analysis produces a 20KB summary that fits in a direct downlink on the same day as the acquisition. Tactical summaries delivered on these timescales could be a significant benefit for exploration since they would arrive in time to help plan followup measurements and navigation decisions for the next command. Independently, they could also inform selective downlink of full data from the most interesting scenes. The following sections describe the onboard processing steps in greater detail.

A. Preprocessing

The Hyperion spectrum contains 220 bands from two detectors. One covers the Visible and Visible Near Infrared (VNIR) and the other covers the Short Wave Infrared (SWIR). Some of these bands can be made accessible to the flight computer through a procedure that loads them into an accessible memory area. This space is limited so only 12 bands can be analyzed onboard at one time. Additionally, it is a software system requirement that one band be included from both detectors. We found noise and reflectance differed dramatically between the two detectors. This impacts analyses based on Euclidean spectral distance since one detector always dominates the other. Fortunately both detectors contain atmospheric absorption features, the values of which are set to zero. Thus we solve the two-detector problem by assigning a single dedicated channel to one of these zeroed frequencies. This leaves a free budget of 11 bands for onboard spectral analysis in the other detector. It ensures data remains well scaled, and satisfies system constraints.

Our experiments evaluate two band selections: a VNIR and SWIR band set, with 11 effective bands each (Table I). We inspected previous Hyperion images to find frequencies that were least prone to artifacts such as pushbroom column stripes, and favored these clean channels. Otherwise we spaced the band selection within each window to evenly cover spectral regions having significant biological and mineralogical absorption features. Exploration missions with particular target materials could optimize band selection to more specific spectral signatures, improving sensitivity at some cost to generality.

The onboard algorithm first converts the initial EO-1 radiance image into a *pseudo-reflectance* product using the procedure of Knapp [46]. This transformation assumes a nominal solar spectrum and a simple Lambertian surface. For a hyperspectral pseudo-reflectance image $I_{j\lambda}$ with pixel j and channel λ we use the following reflectance correction based on reflected radiance L_λ from the image data. This is a function of both solar zenith θ and look angle ϕ, and irradiance from a nominal solar spectrum F_λ :

$$I_{j\lambda} = \frac{L_\lambda(\theta, \phi)}{F_\lambda \cos \theta} \qquad (2)$$

We compute solar irradiance separately for each channel. The total irradiance F_λ also incorporates an Earth/Sun distance that depends on the date of acquisition. We do not consider scene-to-scene or cross-track differences in channel centers. On-orbit calibrations suggest these are less than 5 nm [47], and the solar input model is smooth enough that such differences are not significant. The solar correction procedure is identical to the flight routines used by previous classifiers onboard EO-1 [28], [48]. The onboard memory permits an image of size 256×1024 (256 columns, 1024 rows), and all subsequent analyses presume subframes of this size.

B. Superpixel Segmentation

The next step transforms the pseudo-reflectance image I into a segmented representation by partitioning it into a disjoint set of pixel clusters. Each of these segments, or

VNIR Band	nm	SWIR Band	nm
16	508.2	196	2113.0
20	548.9	198	2133.2
25	599.8	202	2173.5
30	650.7	204	2193.7
33	681.2	205	2203.8
36	711.7	207	2224.0
39	742.3	208	2234.1
42	772.8	211	2264.3
45	803.3	214	2294.6
48	833.8	219	2345.1
52	874.5	221	2365.2

TABLE I

BAND SELECTIONS AND WAVELENGTHS FOR VNIR AND SWIR SCENES.
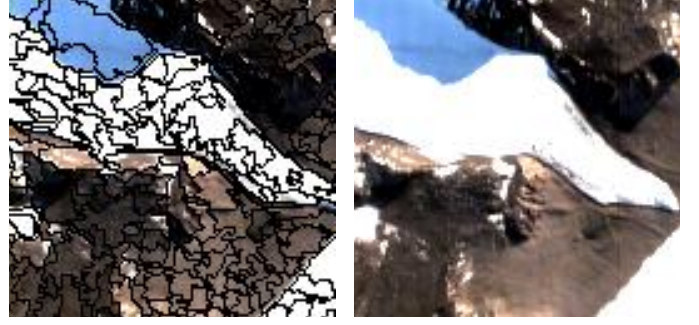ALL WAVELENGTHS ARE GIVEN IN NM.

Fig. 2.   A small portion of Taylor glacier (R: 650.6nm, G: 599.8nm, B: 548.9nm) showing a superpixel segmentation of the 11 VNIR bands. Segments cover contiguous regions that are spectrally homogeneous. Segmentation parameters are identical to those which ran onboard.

superpixels, contains multiple contiguous image pixels I_j that are spectrally similar. The details of this process have been described in previous work [23], [24]. In brief, the segmentation shatters the pixel grid into an 8-connected graph with nodes connected by arcs representing Euclidean spectral distance, and then iteratively joins those nodes using an agglomerative clustering algorithm [49]. Other segmentation and spatial smoothing strategies include Markov Random Fields [50], watershed methods [51], or anisotropic diffusion [52]. Here we found graph agglomeration offered a good balance of reliability, simplicity and speed.

For each clustering iteration the internal difference of a segment S is the largest weight in the segment's minimum spanning tree, $\text{MST}(S)$, biased by a size term based on the area $|S|$. For user-selectable constant β:

$$d_{int}(S) = \max_{(I_i, I_j) \in MST(S)} \|I_i - I_j\|_2 \; + \; \frac{\beta}{|S|} \qquad (3)$$

The between-segment distance denotes the similarity of adjacent clusters S_a and S_b. It is the minimum spectral distance between any of the pixels on the boundary. We define a boundary set $B(S_a, S_b)$ for all neighboring pixels $I_i \in S_a$ and $I_j \in S_b$. The between-segment distance is:

$$d_{bet}(S_a, S_b) = \min_{(I_i, I_j) \in B(S_a, S_b)} \|I_i - I_j\|_2 \qquad (4)$$

We merge clusters according to the Felzenszwalb method [49] that merges neighboring regions when the between-segment distance is smaller than the minimum of either internal weight, e.g. when the following criterion is satisfied:

$$d_{bet}(S_a, S_b) < \min(d_{int}(S_a), d_{int}(S_b)) \qquad (5)$$

The main advantage of this method is that it scales linearly when edges are sorted by weight, or $n \log n$ in the general case where n is the number of pixels. A relatively stable parameter β controls superpixel size. We set β to produce segments with areas of approximately 100. We also enforce a minimum superpixel area of 20, merging smaller regions to their nearest adjacent clusters in a final cleaning step as per [49]. This size range was determined on test images

to provide consistent performance across scenes, balancing noise-robustness and sensitivity to small features. We set these segmentation parameter values once, and then held them constant for all EO-1 experimental trials.

The mean spectra s of all superpixels S form a new representation for the image, reducing the number of data points for later processing.

$$s \; = \; \frac{1}{|S|} \sum_{I_i \in S} I_i \; = \; \mathbf{Eu} + \mathcal{N} \qquad (6)$$

This leads to multiplicative speed benefits, and makes endmember detection suitable for use on EO-1. It guarantees a data set reduction by an order of magnitude at the outset, with considerable reduction in noise outliers (Figure 2). In practice, the spatial averaging improves the robustness of later processing and is critical for accurate endmember extraction in the presence of noise [23]. The superpixels themselves are more credible spectral averages over contiguous physical areas of the surface, improving the interpretability of the result.

C. Endmember Detection

The next step selects superpixels to form the set of endmembers $E = \{e_1, \ldots e_n\}$. We use a Sequential Maximum Angle Convex Cone (SMACC) method [53], similar to Gram Schmidt Orthogonalization. It sequentially selects superpixels to maximize the angular projection onto an ever-growing convex cone of endmembers. As in [53], we initialize the endmember set $E = \{e_1\}$ to contain the superpixel whose mean spectrum s has the largest norm, and then remove it from all remaining superpixel spectra by projection:

$$s' = s - e_1 \psi_1 \frac{se_1}{|e_1|}$$

This is an orthogonal projection if $\psi_1 = 1$ or an oblique projection for the more general case of $0 \leq \psi \leq 1$. We continue this process with subsequent iterations, sequentially adding vectors with maximum residuals to the expanding basis set, updating the projections while maintaining the constraint that $\psi \geq 0$ for all pixels and basis vectors so that the result is physically interpretable in terms of mixing quantities. The result is a set of endmembers of which the other spectra in the scene are convex combinations. This satisfies the original

linear mixing model. Note that many other endmember detection algorithms might work for this stage, but SMACC has the specific advantage of being a sequential method that can return variable numbers of endmembers in rank-ordered priority. Additionally, it is deterministic and therefore reproducible.

Ground operations can still play an important role in interpreting the resulting endmember spectra. The endmember detection method rests on a *pure pixel* assumption, i.e. it cannot infer mixed subpixel components. Instead it returns the most distinctive instances of the spectral signatures where they appear in the image. This still allows manual subpixel interpretation on the ground, where one can identify trace materials having sufficiently distinctive spectral features. Analyst interpretation is also helpful to recognize redundant endmembers. In this work we retrieve an over-complete set of 30 endmembers. This is much larger than the actual intrinsic dimensionality of the data or the number of distinct materials we expect [54]. A large conservative set compensates for the simplicity of the linear mixing model and the fact that SMACC may detect extra materials through differences in illumination, thermal emissivity (for SWIR bands), instrument or continuum effects. For example, uncorrected spectral smile occasionally causes extra endmembers at the edge of the Hyperion swath. Intentionally overestimating the number of endmembers ensures that these redundant bases do not crowd out more numerically subtle (but compositionally distinct) spectra. Extra endmembers also give a margin of error to handle numerical outliers in shadowed or cloudy areas. These redundant endmembers cost relatively little bandwidth, since the resulting classification map has a bit depth that grows with the logarithm of the total number of endmembers. One can easily recognize duplicates or outliers by inspecting the spectra and their matching areas in the scene.

D. Mapping

In the final stage of processing, the onboard system generates a simple scene summary based on the spectral angle (a normalized dot product) between each superpixel spectrum and each endmember spectrum [55]. This indicates the spatial extent of observed features but avoids the computational complexity of a full spectral unmixing [36]. We compute an integer-valued composition map with an index c_i for each superpixel I_i. This is the index of the endmember that is spectrally closest to that superpixel.

$$c_i = \operatorname{argmin}_j \frac{e_j s_i}{\|e_j\|\|s_i\|} \qquad (7)$$

The onboard system communicates this integer composition map, along with the locations and spectra associated with the endmember superpixels. Together these allow the analyst to reconstruct an approximate map of all the spectra in the scene using a data product approximately 20KB in total volume. Each pixel's integer classification requires just 5 bits, and it is highly compressible due to the contiguity of the labeled image regions.

Each stage of processing required special care to satisfy EO-1 onboard memory and processing constraints. The flight computer carries a Mongoose-V 32-bit microprocessor clocked at 12 MHz. It lacks a hardware floating point unit, so all calculations involving decimal numbers must be implemented purely in software emulation. Also, onboard data analysis and autonomy tasks must share the processor with the spacecraft control and flight operations tasks. Onboard memory capacity constrains both specific data analysis tasks and the amount of Hyperion data that may be processed.

III. EVALUATION

A. Scenes

We consider the period from September 2011 to February 2012, during which the system performed six distinct acquisitions. These overflights imaged four different locations:

1) Cuprite, Nevada: The Cuprite mining district has been well-studied from air, space, and ground. It has become a benchmark standard for comparing hyperspectral detection performance. Here we use it to characterize detection performance as well as mapping fidelity in a region with multiple distinctive mineral classes. Cuprite is an acid-sulfate hydrothermal system exhibiting well-exposed kaolinite, alunite, muscovite, and calcite, as well as some silica [56]. All minerals have distinctive and unique absorption features in the 2.1-2.4μm range, so we use the SWIR band set. We commanded two overflights on 19 and 27 September 2011. Both observed the scene with virtually cloudless conditions.

2) Steamboat Hot Springs, Nevada: Steamboat Hot Springs are an active volcanic geothermal area with a long history of remote and *in situ* observations [57], [58]. The exposed structure consists of a hydrothermal silica feature. Of relevance to remote sensing, spectral signatures of alunite and kaolinite are also present [58]. These features have been extensively mapped from both AVIRIS and Hyperion data, and we use these maps as a ground truth standard for onboard analysis. This EO-1 overflight aimed to detect and map the silica sinter and alunite features. We favored the SWIR band set where both kinds of minerals have distinctive absorption signatures. A single trial took place with acquisition over moderately cloudy skies (30% cloud cover).

3) Mammoth Hot Springs, Wyoming: Mammoth Hot Springs is located in Yellowstone national park [59]. It consists of a thermal springs system with nearby pools and streams occupied by etxtremophilic bacteria. This makes the site an interesting astrobiology analogue. The bacterial colonies have features visible in the EO-1 VNIR band set. However, we calculated in advance that their absorbing area would only subtend a very small fraction of the 30m Hyperion pixel, and instead expected to see the entire hot springs system as a single feature. This evaluates the system for the role of detecting a small, isolated but compositionally-distinctive region in a large scene. Two overflights observed the scene under very different cloud conditions; the first took place under clear skies, while the second had cloud cover of 70%. The sinter feature was visible in both scenes, which provides an interesting comparison of the effect of clouds on VNIR scene analysis.

4) Blood Falls, Antarctica: Blood Falls gets its name from the bright red color of oxidized iron staining the ice at the northern terminus of Taylor Glacier in the McMurdo Dry Valleys of Antarctica. The iron source is an intermittent highly saline discharge from a subglacial brine. Iron released by Blood Falls is actually reduced, which is likely related to a microbial consortium that reduces iron as part of a catalytic sulfur cycle [60]. Contact with the air oxidizes the iron and leads to a visible signature of the discharge within VNIR spectral regions. Isolated subglacial ecosystems such as these are astrobiology analogs for potential cold-wet habitats on both Mars and Europa [61], [62]. Recent reanalysis of "chaos" regions on Europa suggest that brine from below the ice shell may be percolating through to the top of the ice as part of the active resurfacing in these areas, possibly allowing similar discharges to those observed at Blood Falls [63]. Therefore, remote detection of signatures from these and other analog environments is critical for planning life detection missions to cold targets [30]. In addition, from a detection standpoint, Blood Falls (like Mammoth Hot Springs) provides a test for detecting a small, isolated anomalous feature of interest in a large scene without prior knowledge of the target spectrum.

Due to the season the solar incidence angle was generally low (~ 45 degrees) causing suboptimal signal to noise for *all* images. This makes target detection difficult; analysts have noticed mixed mapping performance from Hyperion under comparable SNR conditions [64]. Table III shows imaging conditions for each scene, with Signal to Noise Ratio calculated using local means as in the Gao method [65]. The only significant operator-tuned parameters of the onboard analysis are the band selection and the segmentation settings. We set the segmentation parameters in advance using previous Hyperion images of Cuprite, and held them constant across all experiment runs and locations. Table III also reports Look Angle (LA), Solar Zenith Angle (SZA), and Cloud Cover (CC) values from the Hyperion catalog. Finally, Table II shows the target positions as well as data product IDs and runtimes for the total algorithm (T_{Tot}), segmentation (T_{Seg}), and endmember detection (T_{SMACC}) stages.

The time required for the onboard analysis varies widely, even for constant-time operations such as the SMACC endmember detection. Data-handling operations, preprocessing, and preparation of the final summary data products all contribute to the total runtime. We attribute the variable runtimes to concurrent processor usage by other tasks, rather than intrinsic variability in the algorithm. The segmentation operation of the Blood falls run took an unusually long time, which is likely caused by additional processes taking processor priority during this critical polar phase of the EO-1 orbit.

B. Results

We examined the fidelity and interpretability of the telemetry summary products. We transformed the telemetry into draft mineralogical maps by identifying key spectra from the set of 30 returned endmembers, and coloring all the pixels in the downlinked image which had been assigned to that class. Figure 3 below shows the result for the two Cuprite runs. The

colors match a previous map by Kruse et al. [54], [64], generated through spectral endmember identification and MTMF mapping; these maps are reprinted here for comparsion. The two maps demonstrate that automatic discovery of Alunite (A, D) and muscovite features (B, F, G) is most reliable across the two images. Intermittant calcite (C, H) and kaolinite signatures (D,E,G) also appear. The alunite endmember is highly prominent in this band selection, and appears as the second endmember for each run. Figure 4 shows the 11-band endmember spectra associated with these regions, computed and downlinked in telemetry.
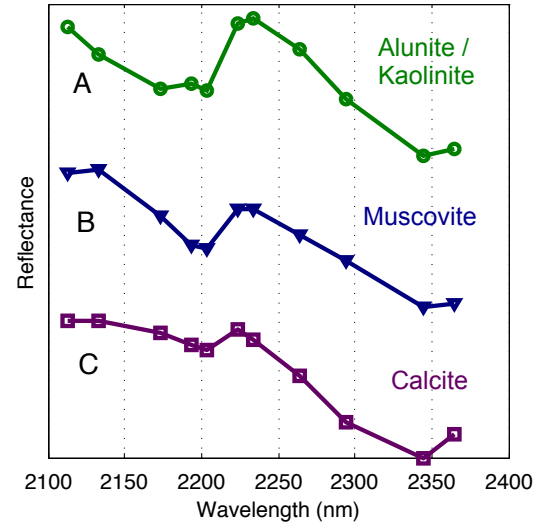

Fig. 4. Cuprite spectra for the first run. We show the mineralogically relevant subset here, excluding endmembers that are obviously noisy, neutral or redundant.

While the returned 11-band spectra show diverse content, their spectral coverage makes it difficult to verify some diagnostic features such as the alunite absorption at 2300nm. To support our physical interpretation we computed the full spectrum on the ground. System constraints mean that just one row and column value are transmitted indicating the location of each endmember superpixel; its shape is unknown so we cannot exactly reconstruct the full endmember spectrum. However, we estimate it here by averaging the full spectra all the matching pixels in the integer map. Specifically we use the average full spectrum of the pixels in the 220-band reflectance data that are located within 50 pixels of the row, column target, and that match best to the appropriate endmember in the automated map. This yields a complete spectrum for the endmember, and suggests the results that might be expected from a followup acquisition, or even in immediate telemetry if the spacecraft were configured with onboard access to the full-spectrum data. The dotted lines in Figure 5 show these reconstructions. To assist interpretation we align the downlinked spectra with a vertical contrast stretch to match the vertical range of the full spectrum result.

The full spectra are consistent with the mineral classes for each of the minerals in the cuprite scene. In particular, absorption features of alunite, calcite, muscovite, and potentially kaolinite are visible in both the quicklook and the full

Target	Lat	Lon	Date	T_{Tot}	T_{Seg}	T_{SMACC}	ID
1. Cuprite	37.566	-117.200	19 Sep 2011	274.7m	172.1m	46.9m	EO1H0410342011262110KF
2. Cuprite	37.566	-117.200	27 Sep 2011	229.2	134.4	54.4	EO1H0410342011270110KF
3. Steamboat	39.39	-119.75	3 Oct 2011	238.3	158.0	40.5	EO1H0430322011276110KF
4. Mammoth	44.969	-110.706	20 Oct 2011	215.1	141.7	39.7	EO1H0380292011293110PF
5. Mammoth	44.969	-110.706	25 Oct 2011	267.4	154.5	59.0	EO1H0380292011298110KF
6. Blood Falls	-77.722	162.274	7 Feb 2012	634.2	569.8	34.4	EO1H0571152012038110KF

TABLE II

SCENE LOCATIONS, RUN TIMES (IN MINUTES), AND PRODUCT IDs.

Target	Bands	SNR	LA	SZA	CC	Detections (Rank)
1. Cuprite	SWIR	19.97	-22.28	43.27	0%	Alunite (2) Muscovite (3), Calcite (27)
2. Cuprite	SWIR	18.63	-8.64	44.70	0%	Alunite (2), Muscovite (16), Calcite (7), Kaolinite(29)
3. Steamboat	SWIR	7.49	22.24	46.36	30%	Silica Sinter (7), Alunite/Kaolinite (22)
4. Mammoth	VNIR	11.96	-2.62	57.94	0%	Thermal springs (1)
5. Mammoth	VNIR	7.42	-13.93	60.06	70%	None (failure)
6. Blood Falls	VNIR	8.02	2.09	71.55	0%	Glacial outflow (27)

TABLE III

PARAMETERIZATION, IMAGING CONDITIONS, AND DETECTIONS. WE REPORT EMPIRICAL SIGNAL TO NOISE (SNR), LOOK ANGLE (LA), SOLAR ZENITH ANGLE (SZA), AND CLOUD COVER (CC)
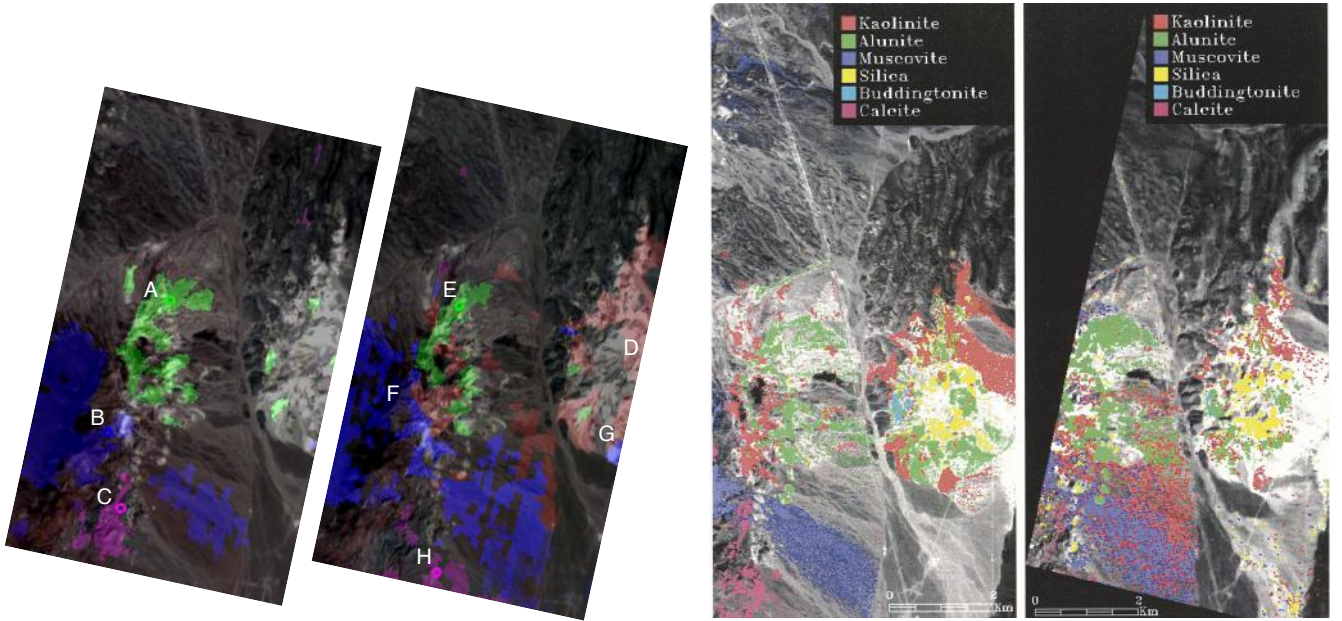

Fig. 3. Mineral maps of Cuprite, Nevada. Left, Left Center: Automated map generated by the EO-1 onboard data analysis and downlinked to the ground. Right Center: Map of Cuprite, Nevada by Kruse et al. using AVIRIS airborne data [54]. Right: Map of Cuprite from Kruse et al. using Hyperion Data.

spectrum. Kaolinite and alunite are often mixed together in the same detection. While there is poor spectral coverage of the alunite absorption feature at 2300nm, the shape of the 2200um absorption feature helps to distinguish this spectrum from pure kaolinite. The detection is consistent across both cuprite scenes. Table IV reports spectral angle distances between spectra in the two cuprite maps. The map's endmember spectra downlinked from EO-1 on the second overflight all match to appropriate spectra in the first overflight, and vice versa. This match uses the 11-band pseudo-reflectance spectra transmitted

within a few hours of acquisition.

Figure 6 shows a similar comparison for the Steamboat Springs run. We produce the map using the quicklook downlink as before. Two endmembers from the list correspond well with kaolinite/alunite (I) and hydrothermal sinter (J) features. A small cloud is visible in the upper portion of the image. We provide another image from the Kruse et al. work, generated using spectral endmember identification and MTMF mapping [64]. This run evidences good agreement with both the mineralogical content as well as the morphology of the
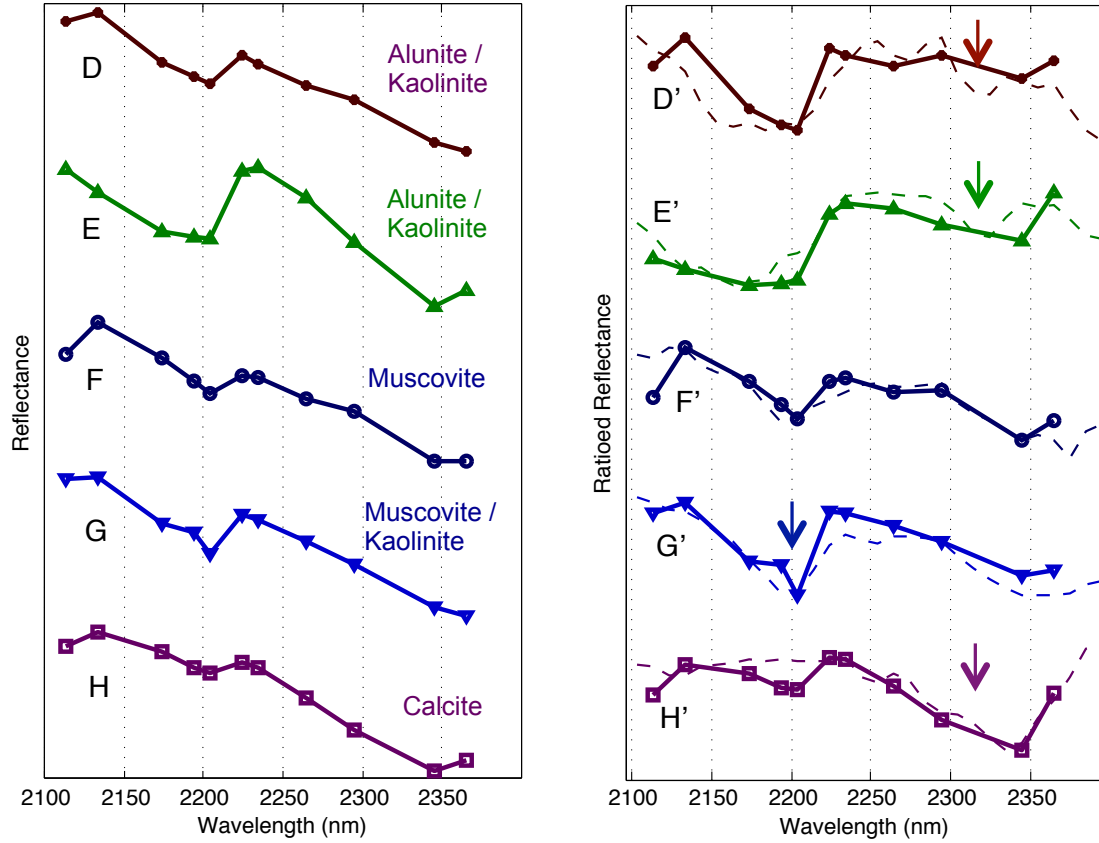
Fig. 5. Cuprite spectra for the second run. Left: reflectance spectra transmitted from the spacecraft. Right: Full reflectance spectra. Dotted lines show the full spectrum associated with their map regions in the reflectance data computed from the full downlink. They verify some spectral features that are not obvious in the 11 band quicklook, such as the alunite absorption at 2300nm.

	D. Alunite	E. Kaolinite	F. Muscovite 1	G. Muscovite	H. Calcite
A. Calcite	0.098	0.072	0.082	0.082	**0.038**
B. Muscovite	0.130	0.071	**0.047**	**0.071**	0.091
C. Alunite	**0.015**	0.142	0.114	0.142	0.126

TABLE IV
SPECTRAL ANGLE MEASURED BETWEEN ASSOCIATED 11-BAND SIGNATURES IN THE TWO CUPRITE RUNS.

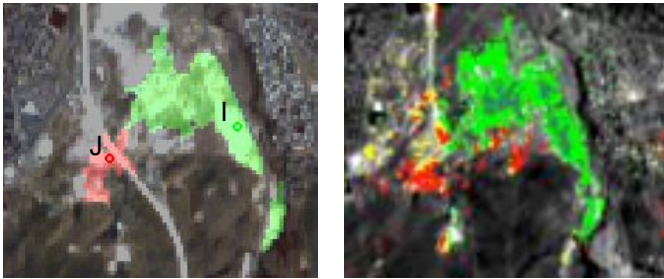two mineral regions. Figure 7 shows the resulting spectra.

Fig. 6. Left: Automated map generated by the EO-1 onboard data analysis and downlinked to the ground. Right: A previous map by the analyses of Kruse et al. using the Mixture Tuned Matched Filter (MTMF) approach [64].

Figure 8 shows the result of run 4 over Mammoth Hot Springs in Yellowstone. Previous studies of this area at $2.1 - 2.4\mu$m have revealed a carbonate (CO_3) feature in the SWIR [59]. Here we use VNIR bands, similar to previous field studies by Hellman et al. [66]. The EO-1 onboard system overflies the target, and detects this small region as the most significant endmember in the scene. As expected, the detection has segmented the Mammoth Falls terraces into multiple superpixels, averaging their spectra and precluding detection of subtler subpixel extremophile signatures. However, the overall morphology and position is a good match to the hot springs feature. The right panel shows a view from the ground. A repeat overflight with 70% cloud cover failed to detect the hot springs; the feature's location was assigned to the 30th endmember which was located elsewhere in the scene. Cloud features dominated the detection results for that run. These stand out numerically due to their high albedo and spectral variability.

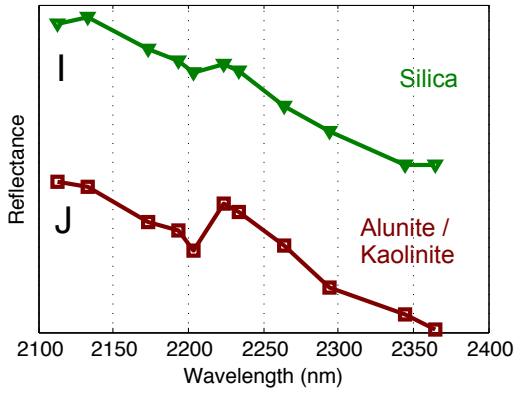Finally, figure 9 shows the detection result for Blood Falls,

Fig. 7. Steamboat springs endmember spectra.

Antarctica. The inset panel shows the outflow as viewed from the context image (left), the downlinked map (center), and the ground (right). The system successfully detects the target, finding a unique endmember at the expected outflow location. This endmember also matches a to a second superpixel on the opposite side of the channel (not shown here). It is possible that this second site is a concentration of iron oxides pooling at the opposite shore.

IV. DISCUSSION

The initial experiments show promise for discovery and mapping of novel mineralogy as well as transient non-mineralogical phenomena. The system manages this result despite modest computational resources and a 20KB downlink limit. Such constraints are not intrinsic to the approach and relaxing them slightly would permit some obvious enhancements. It would be natural to add a confidence score showing the strength of each superpixel's best match. This would add small marginal bandwidth cost, but an indication of ambiguous regions could significantly improve interpretability. Using the full spectral range could improve performance of the segmentation, detection, and downlink stages.

Such analyses could already be feasible for spacecraft with modern flight processors and floating-point hardware. Future implementations could further reduce run times by exploiting more recent avionics systems and specialized hardware. For example, coprocessor implementations of unmixing algorithms have already been tested extensively on ground-side processing [16], [17]. A coprocessor to estimate abundance ratios could enable an even more powerful and informative summary product [18]. Segmentation and endmember detection have parallelizable variants, making the analysis suitable for next-generation parallel computing architectures such as multi-core systems. Multi-core architectures offer a fluid pool of computing resources that could be directed as needed to standard compression or spectral discovery.

More generally, the EO-1 experiments represent just one extreme point on a trade space of bandwidth solutions with different complexity and resource requirements. Table V shows a non-exhaustive list. At one extreme, state of the art compression methods provide compression ratios up to 2-3

[67]. Recent algorithms include the Fast Lossless approach of Arnanki et al [21] that was specifically designed for hyperspectral imagery, and has been evaluated in groundside FPGA testbeds. Lossy compression techniques that do not exploit endmember discovery provide compression ratios up to 20 or more [20], [68]. These approaches are typically based on wavelet decompositions or vector quantization. Several have been implemented in FPGAs, though current missions typically perform compression using the main flight processor.

Regardless of the computing architecture onboard feature detection and mapping could play a complementary role alongside conventional compression methods. Immediately after acquisition, onboard processing could localize novel features to trigger opportunistic followup actions. For instance, mission operators could specify target signatures deserving additional data collection [33]. Alternatively, missions could cultivate a library of observed spectra and trigger followup actions for any novel signals. Such approaches could respond to time-critical science opportunities despite intermittent communications and light time delays. At downlink, scene summary products could reduce data volumes an order of magnitude or more beyond typical lossy compression. These summaries could help prioritize the eventual downlink of full data cubes using more typical compression strategies.

V. CONCLUSION

Imaging spectrometers can play a key role in planetary exploration. However, communications delays and bandwidth limits mean that spacecraft autonomy will be important to realize their full potential. To our knowledge, the experiments described here are the first instance of autonomous spacecraft detection of spectral endmembers, and the first hyperspectral mineralogical mapping onboard a spacecraft. Overall we find that the EO-1 system produces interpretable summaries for sites of mineralogical and astrobiological interest. Identical spacecraft commands discover the key features of interest in multiple different scenes, without foreknowledge of the expected targets. Given system hardware constraints and challenging imaging conditions this first demonstration shows reasonable performance and repeatability. Future research will attempt to realize the concept of adaptive target selection, pairing these purely unsupervised analyses with and more specific detection methods such as background-matched filters for specific signatures. Superpixel representations can improve noise and efficiency for a wide range of onboard analyses as long as computational efficiency remains a primary concern. Many variations are possible, but the EO-1 system serves as an initial proof of concept. Future autonomy of this kind could extend the coverage, duty cycle, and science yield of imaging spectrometers during exploration.

Fig. 8. Mammoth Hot Springs, detected during trial run 4. Left: The entire swath is analyzed. A white inset rectangle shows the location of the center panel, an expanded view of the springs feature. Center: The automated map generated by the EO-1 onboard data analysis and downlinked to the ground. The red region shows area associated with the target endmember. Right: Mammoth Hot Springs, viewed from the ground. Image credit: United States National Park Service slide collection (NPS).
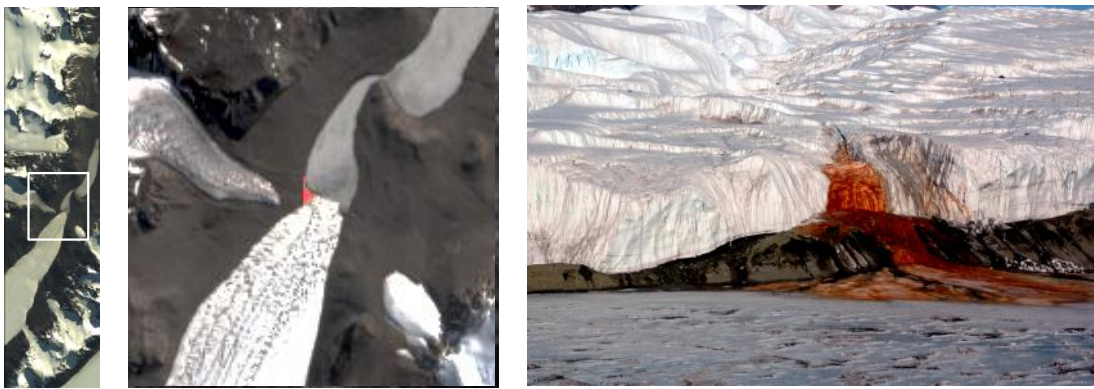

Fig. 9. Blood Falls, Antarctica, detected during trial run 6. Left: The entire swath is searched for endmembers. A white rectangle shows the location of the expanded center panel. Center: the automated map generated by the EO-1 onboard data analysis and downlinked to the ground. The red area shows the region associated with the target endmember. Right: Blood falls as viewed from the surface. Image credit: United States Antarctic Program (USAP).

REFERENCES

[1] R. O. Green, C. M. Pieters, P. Mouroulis, M. Eastwood, J. Boardman, T. Glavich, P. J. Isaacson, M. Annadurai, S. Besse, D. Barr, B. J. Buratti, D. Cate, A. Chatterjee, R. Clark, L. Cheek, J. P. Combe, D. Dhingra, V. Essandoh, S. Geier, J. N. Goswami, R. Green, V. Haemmerle, J. W. H. III, L. Hovland, S. Hyman, R. L. Klima, T. Koch, G. Y. Kramer, A. S. K. Kumar, K. Lee, S. Lundeen, E. Malaret, T. B. McCord, S. McLaughlin, J. F. Mustard, J. W. Nettles, N. E. Petro, K. Plourde, C. Racho, J. Rodriquez, C. Runyon, G. Sellar, C. Smith, H. Sobel, M. I. Staid, J. M. Sunshine, L. A. Taylor, K. Thaisen, S. Tompkins, H. Tseng, G. Vane, P. Varanasi, M. White, , and D. Wilson, "The Moon Mineralogy Mapper (M3) imaging spectrometer for lunar science: Instrument description, calibration, on-orbit measurements, science data calibration and on-orbit validation," *J. Geophys. Res.*, 2011, doi: 10.1029/2011JE003797.

[2] S. Murchie *et al.*, "Compact Reconnaissance Imaging Spectrometer for Mars (CRISM) on Mars Reconnaissance Orbiter," *J. Geophys. Res*, vol. 112, no. 5, 2007.

[3] B. Ehlmann, J. Mustard, S. Murchie, F. Poulet, J. Bishop, A. Brown, W. Calvin, R. Clark, D. Marais, R. Milliken *et al.*, "Orbital identification of carbonate-bearing rocks on Mars," *Science*, vol. 322, no. 5909, p. 1828, 2008.

[4] D. Britt *et al.*, "Asteroids," *Community White Paper to the Planetary Science Decadal Survey, 2011-2020. National Academies Press*, 2010.

[5] D. L. Blaney, P. Mouroulis, R. Green, J. Rodriguez, G. Sellar, B. van Gorp, and D. Wilson, "The Ultra Compact Imaging Spectrometer (UCIS): In situ imaging spectroscopy for Mars, the Moon, and Asteroids," *43rd Lunar and Planetary Sciences Conference*, p. 2593, 2012.

[6] K. Clark, T. Manger, R. Pappalardo, M. Blanc, R. Greeley, J. P. Lebreton, C. Jones, and J. Sommerer, "Jupiter Europa Orbiter Mission Study (Final Report): The NASA Element of the Europa Jupiter System Mission (EJSM)," *NASA/ESA Flagship mission study, Task Order NM0710851, Final Report*, 30 January 2009.

[7] J. Dalton, R. Mogul, H. Kagawa, S. Chan, and C. Jamieson, "Near-infrared detection of potential evidence for microscopic organisms on Europa," *Astrobiology*, vol. 3, no. 3, pp. 505–529, 2003.

[8] D. L. Blaney, R. L. Staehle, B. Betts, L. Friedman, H. Hemmati, M. Lo, P. Mouroulis, P. Pingree, T. Svitek, and T. Wilson, "Interplanetary cubesats: Small, low cost missions beyond low earth orbit," *43rd Lunar and Planetary Sciences Conference*, p. l868, 2012.

[9] D. R. Thompson, D. Wettergreen, and F. Peralta, "Autonomous science during large-scale robotic survey," *Journal of Field Robotics*, vol. 28, no. 4, pp. 542–564, 2011.

[10] T. Estlin, B. Bornstein, D. Gaines, R. C. Anderson, D. R. Thompson, M. Burl, R. C. no, and M. Judd, "Aegis automated targeting for the mer

opportunity rover," *ACM Trans. Intelligent Systems Technology*, 2012 (to appear).

[11] D. R. Thompson, J. Castillo-Rogez, S. A. Chien, R. Doyle, T. Estlin, and D. Mclaren, "Agile science operations: A new approch for primitive bodies exploration," *Proceedings of the SpaceOps Conference, Stockholm, Sweeden*, 2012.

[12] J. Mustard, S. Murchie, S. Pelkey, B. Ehlmann, R. Milliken, J. Grant, J. Bibring, F. Poulet, J. Bishop, E. Dobrea *et al.*, "Hydrated silicate minerals on Mars observed by the Mars Reconnaissance Orbiter CRISM instrument," *Nature*, vol. 454, no. 7202, 2008.

[13] J. L. Bishop, E. Z. Dobrea, N. K. McKeown, M. Parente, B. L. Ehlmann, J. R. Michalski, R. E. Milliken, F. Poulet, G. A. Swayze, J. F. Mustard, S. L. Murchie, and J.-P. P. Bibring, "Phyllosilicate diversity and past aqueous activity revealed at Mawrth Vallis, Mars," *Science*, vol. 321, no. 5890, pp. 830–833, 2008.

[14] D. Valencia, A. Plaza, M. Vega-Rodríguez, and R. Pérez, "FPGA design and implementation of a fast pixel purity index algorithm for endmember extraction in hyperspectral imagery," in *Proceedings of SPIE*, vol. 5995, 2005, pp. 599 508–1.

[15] C. González, J. Resano, D. Mozos, A. Plaza, and D. Valencia, "FPGA implementation of the Pixel Purity Index algorithm for remotely sensed hyperspectral image analysis," *EURASIP Journal on Advances in Signal Processing*, vol. 2010, p. 68, 2010.

[16] C. González, D. Mozos, J. Resano, and A. Plaza, "FPGA Implementation of the N-FINDR algorithm for remotely sensed hyperspectral image analysis," *IEEE Trans. Geosci. Remote Sens.*, no. 99, pp. 1–15, 2012.

[17] A. Plaza, J. Plaza, and H. Vegas, "Improving the performance of hyperspectral image and signal processing algorithms using parallel, distributed and specialized hardware-based systems," *Journal of Signal Processing Systems*, vol. 61, no. 3, pp. 293–315, 2010.

[18] C. González, J. Resano, A. Plaza, and D. Mozos, "Fpga implementation of abundance estimation for spectral unmixing of hyperspectral data using the image space reconstruction algorithm," *IEEE Journal of Selected Topics in Applied Earth Observations and Remote Sensing*, no. 99, pp. 248–261, 2012.

[19] A. Jacobs, C. Conger, and A. George, "Multiparadigm space processing for hyperspectral imaging," in *Aerospace Conference, 2008 IEEE*. IEEE, 2008, pp. 1–11.

[20] T. Fry and S. Hauck, "Spiht image compression on fpgas," *IEEE Trans. Circuits and Systems for Video Tech.*, vol. 15, no. 9, pp. 1138–1147, 2005.

[21] N. Aranki, A. Bakhshi, D. Keymeulen, and M. Klimesh, "Fast and adaptive lossless on-board hyperspectral data compression system for space applications," in *Aerospace conference, 2009 IEEE*, 2009, pp. 1–8.

[22] S. Arnold, R. Nuzzaci, and A. Gordon-Ross, "Energy Budgeting for CubeSats with an Integrated FPGA," *IEEE Aerospace Conference*, 2012.

[23] D. R. Thompson, L. Mandrake, M. S. Gilmore, and R. C. no, "Superpixel endmember detection," *IEEE Trans. Geosci. Remote Sens.*, vol. 40, no. 11, pp. 4023–4033, 2010.

[24] M. S. Gilmore, D. R. Thompson, L. J. Anderson, N. Karamzadeh, L. Mandrake, and R. C. no, "Superpixel segmentation for analysis of hyperspectral data sets, with application to Compact Reconnaissance Imaging Spectrometer for Mars data, Moon Mineralogy Mapper data, and Ariadnes Chaos, Mars," *Journal of Geophysical Research*, vol. 116, E07001, no. doi:10.1029/2010JE003763, 2011.

[25] S. Ungar, J. Pearlman, J. Mendenhall, and D. Reuter, "Overview of the Earth Observing One (EO-1) mission," *IEEE Trans. Geosci. Remote Sens.*, vol. 41, no. 6, p. 11491159, 2003.

[26] S. Chien, R. Sherwood, D. Tran, B. Cichy, G. Rabideau, R. Castano, A. Davies, D. Mandl, S. Frye, B. Trout, S. Shulman, and D. Boyer, "Using autonomy flight software to improve science return on Earth Observing One," *Journal of Aerospace Computing, Information, and Communication*, April 2005.

[27] A. G. Davies and S. Chien and V.Baker and T.Doggett and J.Dohm and R.Greeley and F. Ip and R. Castano and B. Cichy and R. Lee and G. Rabideau and D. Tran and R. Sherwood, "Monitoring active volcanism with the Autonomous Sciencecraft Experiment (ASE)," *Remote Sensing of Environment*, vol. 101, no. 4, pp. 427–446, 2006.

[28] T. Doggett, R. Greeley, A.G. Davies, S. Chien, B. Cichy, R. Castano, K. Williams, V. Baker, J. Dohm, and F. Ip, "Autonomous on-board detection of cryospheric change," *Remote Sensing of Environment*, vol. 101, no. 4, pp. 447–462, 2006.

[29] F.Ip, J.Dohm, V.Baker, T.Doggett, A.G.Davies, R.Castano, S. Chien, B. Cichy, R. Greeley, , and R. Sherwood, "Development and testing of the Autonomous Spacecraft Experiment (ASE) floodwater classifiers:

real-time smart reconnaissance of transient flooding," *Remote Sensing of Environment*, vol. 101, no. 4, pp. 463–481, 2006.

[30] D. Gleeson, R. Pappalardo, S. Grasby, M. Anderson, B. Beauchamp, R. Castano, S. Chien, T. Doggett, L. Mandrake, , and K. Wagstaff, "Characterization of a sulfur-rich arctic spring site and field analog to Europa using hyperspectral data," *Remote Sensing of Environment*, vol. 114, pp. 1297–1311, 2010.

[31] S. Pelkey, J. Mustard, S. Murchie, R. Clancy, M. Wolff, M. Smith, R. Milliken, J. Bibring, A. Gendrin, F. Poulet *et al.*, "CRISM multispectral summary products: Parameterizing mineral diversity on Mars from reflectance," *J. Geophys. Res*, vol. 112, 2007.

[32] R. N. Clark, G. A. Swayze, K. E. Livo, R. F. Kokaly, S. J. Sutley, J. B. Dalton, R. R. McDougal, and C. A. Gent, "Imaging spectroscopy: Earth and planetary remote sensing with the USGS Tetracorder and expert systems," *Journal of Geophysical Research*, vol. 108(E12), 5131, no. doi:10.1029/2002JE001847, 2003.

[33] Bue, B. D. and Meréandnyi, E. and Csathó, B., "Automated labeling of materials in hyperspectral imagery," *Trans. Geosci. Remote Sens.*, vol. 48, no. 11, pp. 4059 –4070, Nov. 2010.

[34] J. W. Boardman and F. A. Kruse, "Analysis of imaging spectrometer data using n-dimensional geometry and a Mixture-Tuned Matched Filtering (MTMF) approach," *Trans. Geosci. Remote Sens.*, vol. 49, pp. 4138–4152, 2011.

[35] A. Plaza, P. Martinez, R. Pérez, and J. Plaza, "A quantitative and comparative analysis of endmember extraction algorithms from hyperspectral data," *IEEE Trans. Geoscience and Remote Sensing*, vol. 42, no. 3, pp. 650–663, 2004.

[36] N. Keshava and J. Mustard, "Spectral unmixing," *Signal Processing Magazine, IEEE*, vol. 19, no. 1, pp. 44–57, 2002.

[37] N. Keshava, "Distance metrics and band selection in hyperspectral processing with applications to material identification and spectral libraries," *IEEE Trans. Geosci. Remote Sens.*, vol. 42, no. 7, pp. 1552–1565, 2004.

[38] J. Bioucas-Dias and A. Plaza, "Hyperspectral unmixing: Geometrical, statistical, and sparse regression-based approaches," in *Proc. SPIE*, vol. 7830, 2010, pp. 78 300A–78 300A.

[39] M. Parente and A. Plaza, "Survey of geometric and statistical unmixing algorithms for hyperspectral images," in *Hyperspectral Image and Signal Processing: Evolution in Remote Sensing (WHISPERS), 2010 2nd Workshop on*. IEEE, 2010, pp. 1–4.

[40] J. Boardman *et al.*, "Automating spectral unmixing of AVIRIS data using convex geometry concepts," in *Summaries 4th Annu. JPL Airborne Geoscience Workshop*, vol. 1, 1993, pp. 11–14.

[41] M. Winter, "N-FINDR: An algorithm for fast autonomous spectral endmember determination in hyperspectral data," in *Proc. SPIE*, vol. 3753, 1999, p. 266.

[42] J. Nascimento and J. Dias, "Vertex component analysis: A fast algorithm to unmix hyperspectral data," *IEEE Trans. Geosci. Remote Sens.*, vol. 43, no. 4, pp. 898–910, 2005.

[43] S. Mei, M. He, Z. Wang, and D. Feng, "Spatial purity based endmember extraction for spectral mixture analysis," *IEEE Trans. Geosci. Remote Sens.*, vol. 48, no. 9, pp. 3434–3445, 2010.

[44] M. Zortea and A. Plaza, "Spatial preprocessing for endmember extraction," *IEEE Trans. Geosci. Remote Sensing*, vol. 47, no. 11, 2009.

[45] D. M. Rogge, B. Rivard, J. Zhang, J. Harris, A. Sanchez, and F. J., "Integration of Spatial-Spectral Information for the Improved Extraction of Endmembers," *Remote Sensing of Environment.*, vol. 110, pp. 287–303, 2008.

[46] K. R. Knapp, "Radiance to reflectance for GOES-8 channel 1," *Tech. Rep., Colorado State University*, August 1996.

[47] R. Green, B. Pavri, and T. Chrien, "On-orbit radiometric and spectral calibration characteristics of EO-1 Hyperion derived with an underflight of AVIRIS and in situ measurements at Salar de Arizaro, Argentina," *IEEE Trans. Geosci. Remote Sens.*, vol. 41, no. 6, pp. 1194–1203, 2003.

[48] L. Mandrake, K. Wagstaff, D. Gleeson, U. Rebbapragada, D. Tran, R. Castano, S. Chien, and R. Pappalardo, "Onboard SVM analysis of Hyperion data to detect sulfur deposits in Arctic regions," *Proceedings of the IEEE WHISPERS Workshop*, 2009.

[49] P. F. Felzenszwalb and D. P. Huttenlocher, "Efficient graph-based image segmentation," *Intl. J. Computer Vision*, vol. 59:2, September 2004.

[50] A. Mohammadpour, O. Féron, and A. Mohammad-Djafari, "Bayesian segmentation of hyperspectral images," *Bayesian Inference and Maximum Entropy Methods in Science and Engineering*, vol. 735, pp. 541–548, 2004.

[51] Y. Tarabalka, J. Chanussot, and J. Benediktsson, "Segmentation and classification of hyperspectral data using watershed transformation," *Pattern Recognition*, vol. 43, no. 7, pp. 2367–2379, 2010.

[52] J. Martin-Herrero, "Anisotropic diffusion in the hypercube," *IEEE Trans. on Geosci. Remote Sensing*, vol. 45, no. 5 Part 2, pp. 1386–1398, 2007.

[53] J. Gruninger, A. Ratkowski, and M. Hoke, "The sequential maximum angle convex cone (SMACC) eUnfortunately, ondmember model," *Proc. SPIE, Algorithms for Multispectral and Hyper-spectral and Ultraspectral Imagery*, vol. 5425, pp. 1–14, 2004.

[54] F. A. Kruse, J. W. Boardman, and J. F. Huntington, "Comparison of airborne hyperspectral data and EO-1 Hyperion for mineral mapping," *IEEE Trans. Geosci. Remote Sens.*, vol. 41, pp. 1388–1400, 2003.

[55] F. A. Kruse, A. B. Lefkoff, J. B. Boardman, K. B. Heidebrecht, A. T. Shapiro, P. J. Barloon, and A. F. H. Goetz, "The Spectral Image Processing System (SIPS) - Interactive visualization and analysis of imaging spectrometer data," *Remote Sensing of Environment*, vol. 44, pp. 144–163, 1993.

[56] G. A. Swayze, "The hydrothermal and structural history of the Cuprite Mining District, Southwestern Nevada: An integrated geological and geophysical approach," *Ph.D. thesis, Univ. Colorado, Boulder, CO*, 1997.

[57] N. L. Nehring, "Geochemistry of steamboat springs, nevada," *USGS Numbered Series Open-File Report, U.S. Geological Survey*, no. 80-887 : USGS (200) R29o no. 80-887, 1980.

[58] F. A. Kruse, "Mapping Hot spring deposits with AVIRIS at Steamboat Springs, Nevada," *Proceedings of the 8th JPL Airborne Earth Science Workshop, Jet Propulsion Laboratory Publication*, vol. 99, no. 17, pp. 239 – 246, 1999.

[59] K. Livo, F. A. Kruse, R. Clark, R. Kokaly, and W. I. Shanks, *Hydrothermally altered rock and hot-spring deposits at Yellowstone National Park characterized using airborne visible- and infrared-spectroscopy Data*. U.S. Geological Survey Professional Paper 1717, http://pubs.usgs.gov/pp/1717/downloads/pdf/p1717O.pdf, 2007, ch. O.

[60] J. Mikucki, C. Foreman, B. Sattler, W. Berry Lyons, and J. Priscu, "Geomicrobiology of Blood Falls: an iron-rich saline discharge at the terminus of the Taylor Glacier, Antarctica," *Aquatic Geochemistry*, vol. 10, no. 3, pp. 199–220, 2004.

[61] A. Fairén, "A cold and wet mars," *Icarus*, vol. 208, no. 1, pp. 165–175, 2010.

[62] G. Marion, C. Fritsen, H. Eicken, and M. Payne, "The search for life on Europa: limiting environmental factors potential habitats and Earth analogues," *Astrobiology*, vol. 3, no. 4, pp. 785–811, 2003.

[63] S. BE, B. DD, P. GW, and S. PM, "Active formation of chaos terrain over shallow subsurface water on Europa," *Nature*, vol. 479, no. 7374, pp. 502–505, 2011.

[64] F. A. Kruse, J. W. Boardman, and J. F. Huntington, *Final Report: Evaluation and geologic validation of EO-1 Hyperion (NASA grant NCC5-495)*. Boulder, CO, 55 pages.: Analytical Imaging and Geophysics, LLC, 2003.

[65] B. Gao, "An operational method for estimating signal to noise ratios from data acquired with imaging spectrometers," *Remote Sensing of Environment*, vol. 43, no. 1, pp. 23–33, 1993.

[66] M. Hellman and M. Ramsey, "Analysis of hot springs and associated deposits in Yellowstone National Park using ASTER and AVIRIS remote sensing," *Journal of volcanology and geothermal research*, vol. 135, no. 1-2, pp. 195–219, 2004.

[67] G. Motta, F. Rizzo, and J. Storer, *Hyperspectral data compression*. Springer-Verlag New York, Inc, 2006.

[68] S. Qian, M. Bergeron, I. Cunningham, L. Gagnon, and A. Hollinger, "Near lossless data compression onboard a hyperspectral satellite," *IEEE Trans. Aerospace and Electronic Systems*, vol. 42, no. 3, pp. 851–866, 2006.

[69] M. Klimesh, "Low-complexity lossless compression of hyperspecral imagery via adaptive filtering," *The Interplanetary Network Progress Report*, vol. 42-163, 2005.

[70] A. Kiely, M. Klimesh, H. Xie, and N. Aranki, "ICER-3D: A progressive wavelet-based compressor for hyperspectral images," *IPN Progress Report*, vol. 42-164, 2006.

[71] X. Tang and W. Pearlman, "Three-dimensional wavelet-based compression of hyperspectral images," *Hyperspectral Data Compression*, pp. 273–308, 2006.

[72] A. Plaza, Q. Du, Y. Chang, and R. King, "High performance computing for hyperspectral remote sensing," *IEEE Journal of Selected Topics in Applied Earth Observations and Remote Sensing*, vol. 4, no. 3, pp. 528–544, 2011.

David R. Thompson received the M.Sc. degree in informatics from the University of Edinburgh, Edinburgh, U.K. and the Ph.D. degree in robotics from the Carnegie Mellon Robotics Institute, Pittsburgh, PA. He is a Researcher in the Machine Learning and Instrument Autonomy group at the Jet Propulsion Laboratory, Pasadena, CA. His work focuses on machine learning and pattern recognition for remote sensing and autonomous planetary science.

Benjamin Bornstein received a B.Sc. in Computer Science from the University of Minnesota Duluth in 1999. He is a senior member of the Machine Learning and Instrument Autonomy group at the Jet Propulsion Laboratory, Pasadena, CA. Ben has over 10 years experience developing onboard science autonomy software for a variety of NASA spacecraft and instruments.

Steve Chien is Technical Group Supervisor of the Artificial Intelligence Group and Principal Computer Scientist in the Mission Planning and Execution Section at the Jet Propulsion Laboratory, California Institute of Technology. He leads efforts in automated planning and scheduling for space exploration. He holds a B.S. with Highest Honors in Computer Science, with minors in Mathematics and Economics, M.S., and Ph.D. degrees in Computer Science, all from the University of Illinois.
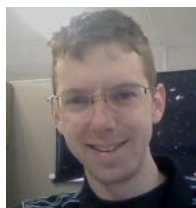
Steven Schaffer has worked for the Jet Propulsion Laboratory's Artificial Intelligence Group as a research programmer since May 2001. He has been involved in automated DSN antenna control and scheduling, executive modelling for research rovers, flight experiment validation, sensorweb operations, autonomous planning under uncertainty, aerobot executive control, onboard science analysis, and mission telemetry analysis. Steve holds bachelors degrees in computer science and chemistry from Carnegie Mellon University.

Daniel Tran is a member of the technical staff in the Artificial Intelligence Group at the Jet Propulsion Laboratory, California Institute of Technology, where he is working on developing automated planning and scheduling systems for onboard spacecraft commanding. Daniel attended the University of Washington and received a B.S. in Computer Engineering. He is currently the software lead for the Autonomous Sciencecraft Experiment, co-winner of the 2005 NASA Software of the Year award.

Brian D. Bue is a Ph.D. student in the department of Electrical and Computer Engineering at Rice University, Houston, TX. He was previously an associate member of the technical staff in the Machine Learning and Instrument Autonomy group at the Jet Propulsion Laboratory, Pasadena, CA. He received the M.S. degree in computer science from Purdue University, West Lafayette, IN. His research involves developing machine learning and pattern recognition techniques for remotely sensed imagery, in particular, hyperspectral imagery, for applications in Earth and planetary science.

Rebecca Castaño received the Ph.D. degree in electrical engineering from the University of Illinois with her dissertation in the area of computer vision. She is currently an Assistant Manager with the Jet Propulsion Laboratory Section for Instrument Software and Science Data Systems. She has been advancing the state of the art in autonomous planetary science and remote sensing analysis for over a decade and has been lead author on numerous publications in the field.

Damhnait F. Gleeson received her M.Sc. in Applied Remote Sensing and GIS from the National University of Ireland Maynooth, and her Ph.D. in Geology from The University of Colorado in Boulder. Previously located at the Jet Propulsion Lab in Pasadena, she is currently a Mars Scientist at the Centro de Astrobiologa in Madrid. She explores the expression of terrestrial field sites analogous to Europa and Mars surface environments across multiple scales of spectral data, with a view to linking large scale biosignatures to microbial activities.

Aaron Noell is a Postdoctoral Scholar at the Jet Propulsion Laboratory. He received a Ph.D in Chemistry from the California Institute of Technology in 2010. His work focuses on the ability of life to remain viable in extreme environments. Additional areas of focus include atmospheric chemistry of earth and other planets, and instrumentation development for life detection.

Method	Compression ratio	Feature detection?	Examples
Lossless (Software)	3-4	N	FL [69]
Lossless (FPGA)	3-4	N	FL [21]
Lossy / Wavelet (Software)	20-30	N	Wavelet/ICER-3D [70]
Lossy / Wavelet (FPGA)	20-30	N	3D-SPECK [71], SPIHT [20]
Endmember Discovery (Software)	>100	Y	This work*
Endmember Discovery (FPGA)	>100	Y	PPI [14], [17], [72], N-FINDR [16]

TABLE V

ALGORITHMS DESIGNED FOR HYPERSPECTRAL IMAGE PROCESSING ONBOARD SPACECRAFT. *DEPLOYMENTS TO SPACEFLIGHT